Chinese Chemical Letters 35 (2024) 108447

Contents lists available at ScienceDirect

Chinese Chemical Letters

journal homepage: www.elsevier.com/locate/cclet

Bi^{3+}-activated dual-wavelength emitting phosphors toward effective optical thermometry

Yu Xue[a], Yuqi Chen[a], Guixian Li[a], Weixi Xia[a], Qinan Mao[a], Lang Pei[a], Meijiao Liu[c], Liang Chu[b,*], Jiasong Zhong[a,*]

[a] Center of Advanced Optoelectronic Materials, College of Materials and Environmental Engineering, Hangzhou Dianzi University, Hangzhou 310018, China
[b] College of Electronics and Information, Hangzhou Dianzi University, Hangzhou 310018, China
[c] Department of Chemistry, Zhejiang Sci-Tech University, Hangzhou 310018, China

ARTICLE INFO

Article history:
Received 21 February 2023
Revised 8 March 2023
Accepted 12 April 2023
Available online 13 April 2023

Keywords:
Dual-wavelength emitting
Cationic substitution
Two local electronic states
Optical thermometry
Bi^{3+}-doped phosphor

ABSTRACT

Optical thermometry as an important local temperature-sensing technique, has received increasing attention in scientific and industrial areas. However, it is still a big challenge to develop luminescent materials with self-activated dual-wavelength emissions toward high-sensitivity optical thermometers. Herein, a novel ratiometric thermometric strategy of Bi^{3+}-activated dual-wavelength emission band was realized in the same lattice position with two local electronic states of $La_3Sb_{1-x}Ta_xO_7:Bi^{3+}(0 \le x \le 1.0)$ materials based on the different temperature-dependent emission behaviors, benefiting from the highly-sensitive and regulable emission to the coordination environment of Bi^{3+}. The structural and spectral results demonstrate that the emission tremendously shifted from green to blue with 68 nm and the intensity was enhanced 2.6 times. Especially, the visual dual-wavelength emitting from two emission centers was presented by increasing the Ta^{5+}substitution concentration to 20% or 25%, mainly originating from the two local electronic states around the Bi^{3+} emission center. Significantly, the dual-wavelength with different thermal-quenching performance provided high-temperature sensitivity and good discrimination signals for optical thermometry in the range between 303 and 493 K. The maximum relative sensitivity reached 2.64%/K ($La_3Sb_{0.8}Ta_{0.2}O_7:0.04Bi^{3+}$@383 K) and 1.91%/K ($La_3Sb_{0.75}Ta_{0.25}O_7:0.04Bi^{3+}$ @388 K). This work reveals a rational design strategy of different local electronic states around the single-doping multiple emission centers towards practical applications, such as luminescence thermometry and white LED lighting.

With the development of science and technology, temperature detection accuracy is highly demanded [1,2]. Luminescence thermometry possesses obvious advantages, such as non-contact, rapid response, noninvasive operation, excellent spatial and temperature resolution [3]. Importantly, this technology can be applied in a complex environment, micro/nano system, and strong electronic/magnetic field [4–7]. Fluorescence intensity ratio (FIR), luminescence lifetime, and emission peak/bandwidth are the main three paradigms of luminescence thermometry [8–11]. In FIR, the calibration curve is determined by the relative ratio of emission peaks or integrated intensity at a certain temperature [12], which is not easily disturbed by non-temperature parameters. The method of the relative ratio of the emission intensities can reduce the systemic error from the fluctuation of the excitation light source to enhance accuracy and repeatability [13,14]. In general, the relative emission peaks are managed by co-doping temperature-sensitive transition metal (TM) and thermally-stable rare earth ions [15]. Besides, the thermal quenching can be tuned by changing the TM crystal field. However, the two-type ions have different excitation wavelengths, weakening the efficiency of temperature detection. To date, it is desired to explore single-doped based dual-wavelength emission phosphor for effective luminescence thermometry [16].

Bismuth (Bi), an important TM element, has attracted increasing attention due to the flexible optical properties of the intimate interaction with the coordination environment [17,18]. Meanwhile, the outside electrons of Bi ($[Xe]4f^{14}5d^{10}6s^26p^3$) are sensitive to the crystal structure and local electronic states [19,20]. Thus, the emission of Bi^{3+}-doped phosphors has wide-range color engineering from ultraviolet (UV) to blue, green, yellow, and even red, by managing the hosts or ligands [21–23]. The PL spectra tunability of Bi^{3+} ions in a single host can be realized through the

* Corresponding authors.
E-mail addresses: chuliang@hdu.edu.cn (L. Chu), jiasongzhong@hdu.edu.cn (J. Zhong).

https://doi.org/10.1016/j.cclet.2023.108447
1001-8417/

following two strategies, cationic substitution to regulate the crystal structure and co-doping activator ions to form the energy transfer [24,25]. However, co-doping is usually complex. And the cationic substitution can manage the crystal field strength of the host to change the luminescence properties [3,26]. In fact, the local electronic states around the luminescent center are affected by the crystal field strength and further influence the emission performance of Bi^{3+} ions. Therefore, the local electronic state modulation around the different emission centers may realize the single-doped Bi^{3+} dual-emitting [27,28].

In this work, an alternative strategy is designed for luminescence thermometry *via* dual-emitting of a single Bi^{3+} vital activator-doped $La_3Sb_{1-x}Ta_xO_7$ ($0 \le x \le 1.0$) matrix. By managing the substitution concentration as 20% and 25%, the Bi^{3+}-doped $La_3Sb_{1-x}Ta_xO_7$ phosphors have obvious two emission peaks at 452 nm and 530 nm under the 303 nm excitation, due to the two emission centers from the corresponding local electronic states. The thermal quenching behaviors can be indicated in the temperature-dependence PL spectra operating from 303 K to 493 K. Based on the fluorescence intensity ratio, the maximum S_r are determined as 2.64%/K ($La_3Sb_{0.8}Ta_{0.2}O_7$:0.04Bi^{3+}@383 K) and 1.91%/K ($La_3Sb_{0.75}Ta_{0.25}O_7$:0.04$Bi^{3+}$@388 K), respectively, which illustrate the potential for luminescence temperature measurement.

Series of La_3SbO_7:yBi^{3+}($0.02 \le y \le 0.12$) and $La_3Sb_{1-x}Ta_xO_7$:0.04Bi^{3+} ($0 \le x \le 1.0$) phosphors were synthesized by a conventional solid-state reaction method. The raw materials of La_2O_3 (99.99%), Sb_2O_5 (99.5%), Ta_2O_5 (99.99%) and Bi_2O_3 (99.99%) were weighed according to the designed stoichiometric ratio, mixed thoroughly in an agate mortar by grounding, and then sintered in a furnace at 1450 °C for 4 h with a heating rate of 5 °C/min in air. After the reaction was cooled to room temperature naturally, the as-prepared phosphors were crushed into tiny powders.

The crystal structure and composition of the phosphors were characterized by X-ray diffraction (XRD) on a Bruker D8 Advance diffractometer (40 kV, 30 mA). Rietveld refinement was performed by the Maud 2.94 program. The morphology and elemental mapping were conducted by scanning electron microscope (SEM, FEI ApreoHiVac) equipped with an energy-dispersive X-ray spectrometer (EDX). The photoluminescence (PL), and photoluminescence excitation (PLE) spectra were characterized using a fluorescence spectrometer (Edinburgh Instrument FS5) with a 150 W continuous xenon lamp. The decay curves were measured by another fluorescence spectrometer (Horiba Fluorolog-3 with a 340 nm laser device). Temperature-dependent PL spectra were measured using an FS5 spectrometer equipped with a homemade temperature controller from 303 K to 493 K. The diffuse reflectance was performed by a UV-3600 spectrophotometer (Shimadzu Corporation, Tokyo, Japan), using the $BaSO_4$ standard reference. X-ray photoelectronic spectroscopy (XPS) spectra were performed on Thermo Scientific K-Alpha.

The fluorite-related structure of the compound (La_3SbO_7, $La_3Sb_{1-x}Ta_xO_7$) belongs to the orthorhombic crystal. There are two sites of La^{3+} with coordinates of [La1O_8] and [La2O_7] (Fig. 1). Based on the same coordination number and similar radius of Bi^{3+} (r = 1.17 Å) and La^{3+}(r = 1.16 Å), Bi^{3+} is supposed to replace the site of [La1O_8] rather than the sites of [La2O_7] and [SbO_6], because Bi ions cannot be doped into structures with seven coordination number. [29] The similar crystal structure of La_3SbO_7 and La_3TaO_7 makes the possibility of Ta/Sb cationic substitution. In general, the ion terms spilled into several sub-levels with large energy differences due to the nephelauxetic effect of doping Bi^{3+} ions into the host lattice. And the cationic substitution greatly affects the crystal field (CF) splitting of Bi^{3+} ions to adjust the luminescence performance of Bi^{3+}. As the Ta^{5+} (r = 0.64 Å) substitutes for Sb^{5+} (r = 0.60 Å) in $[MO_6]^{7-}$, the lattice can expanse due to the bigger ionic radius of Ta^{5+}. Meanwhile, the modulation of the crystal field and nephelauxetic effect can change the peak position and intensity in the PL spectra.

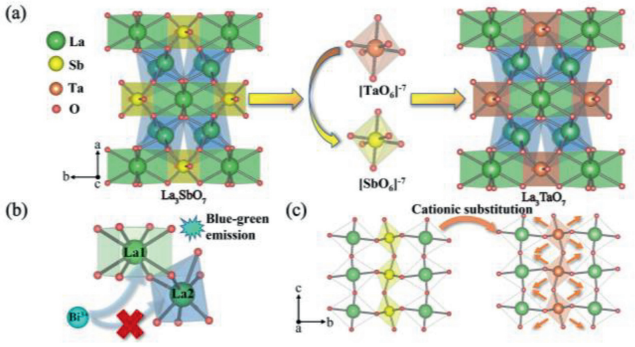

Fig. 1. Crystal-structural of La_3SbO_7:Bi^{3+}. (a) Unit cell structures of La_3SbO_7 and La_3TaO_7. (b) Schematic diagram of Bi^{3+} doping in La1 position. (c) Schematic diagram of the substitution process.

To verify the phase and crystal structure of La_3SbO_7:yBi^{3+} ($0.02 \le y \le 0.12$) and $La_3Sb_{1-x}Ta_xO_7$:0.04Bi^{3+} ($0 \le x \le 1.0$) phosphors, XRD and Rietveld refinements are demonstrated in Figs. 2a and b. All the diffraction peaks of the obtained Bi^{3+}-doped phosphors are consistent well with the standard cards of La_3SbO_7 (PDF#23–1138) or La_3TaO_7 (PDF#38–1418) without any impurity phases. As presented in Fig. 2b, the diffraction pattern gradually shifts from the crystal structure of La_3SbO_7 to La_3TaO_7 one with increasing the substitution in $La_3Sb_{1-x}Ta_xO_7$:0.04Bi^{3+} ($0 \le x \le 1.0$). Meanwhile, the substitution process produces no other phases or impurities. Besides, the diffraction peaks gradually shift to a lower degree with increasing Ta^{5+} substitution, due to the lattice expansion from the different ionic sizes (Sb^{5+}: 0.60 Å, Ta^{5+}: 0.64 Å). Moreover, XRD rietveld refinements elucidate the detailed crystal structure data of $La_3Sb_{1-x}Ta_xO_7$:0.04Bi^{3+} ($0 \le x \le 1.0$) (Figs. 2c-f, Figs. S1-S4 and Table S1 in Supporting information). Following Vegard's law, the crystal structural parameters present a linear incremental with Ta^{5+} substitution increasing, agreeing with the lattice expansion.

The SEM image and related elemental mapping diagrams of $La_3Sb_{0.75}Ta_{0.25}O_7$:0.04$Bi^{3+}$ phosphors are demonstrated in Fig. 2g. The mean particle size is about 5 μm. The elemental mapping further confirms the element La, Sb, Ta, O and Bi are homogeneously scattered in the selected region. All the coherent elements are displayed in the EDX spectrum (Fig. S5 in Supporting information), and the element mass proportion in accordance with the chemical formula, further proves the uniform distribution of Ta^{5+} ions as the partial substitution for Sb^{5+} ions.

Diffuse reflection spectra are evaluated in Fig. 3a. Notably, the Bi^{3+}-doped samples have obvious absorption peaks between 290 nm and 380 nm, in good agreement with the excitation peak of PLE spectra. In addition, the bandgaps can be estimated through the Kubelka-Munk functions [30]:

$$F(R) = (1-R)^2/2R \quad (1)$$

$$[F(R) \times h\nu]^2 = A(h\nu - E_g) \quad (2)$$

where $F(R)$ is the absorption, R is the reflectance (%), $h\nu$ is the photon energy, and E_g is the bandgap. The E_g values of La_3SbO_7, $La_3Sb_{0.75}Ta_{0.25}O_7$ and La_3TaO_7 are calculated as 4.86, 4.92 and 5.03 eV, respectively, stemming from the linear part of the absorption curve (Fig. S6 in Supporting information). Obviously, the bandgaps gradually enhanced with increasing substitution of Ta^{5+} in La_3SbO_7 host. Bismuth cations could easily exist with different

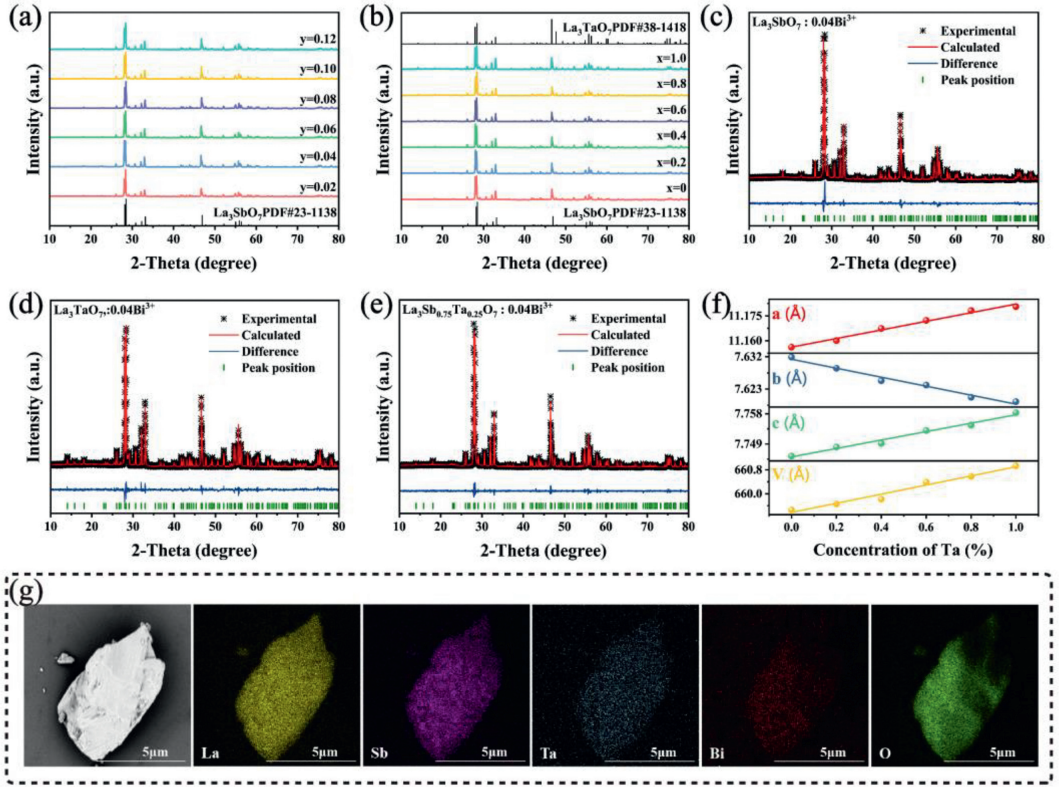

Fig. 2. Crystal phase of La_3SbO_7:Bi^{3+}. (a, b) XRD patterns of La_3SbO_7:yBi^{3+} ($0.02 \le y \le 0.12$) and $La_3Sb_{1-x}Ta_xO_7$:0.04Bi^{3+} ($0 \le x \le 1.0$). (c-e) XRD Rietveld refinements of La_3SbO_7:0.04Bi^{3+} and La_3TaO_7:0.04Bi^{3+} and $La_3Sb_{0.75}Ta_{0.25}O_7$:0.04$Bi^{3+}$. (f) Summary of cell parameters. (g) SEM and corresponding elemental mapping images of $La_3Sb_{0.75}Ta_{0.25}O_7$:0.04$Bi^{3+}$.

valence states in solid compounds, which greatly affect the luminescent properties. The X-ray photoelectron spectroscopy confirms the Bi^{3+} state in La_3SbO_7:0.04Bi^{3+}, $La_3Sb_{0.75}Ta_{0.25}O_7$:0.04$Bi^{3+}$ and La_3TaO_7:0.04Bi^{3+}. The two characteristic peaks of Bi^{3+} at 164 eV and 159 eV come from the respective $4f_{5/2}$ and $4f_{7/2}$ of Bi^{3+} in the phosphors (Fig. 3b). Additionally, the peak of the 4f orbit shifts to lower energy, with the same trend as the characteristic peak of the O 1s orbital (Figs. 3b and c). The peak shift can be ascribed to the transformation of the local electronic state, resulting from the cationic substitution [31,32].

To explore the doping concentration on the luminescence properties, PL spectra are demonstrated in Fig. 3d. According to the emission spectrum and intensity integration, the optimum concentration of Bi^{3+} can be estimated as 0.04. The emission intensity decreases as increasing of Bi^{3+} concentration due to the concentration quenching, which is mainly originated from the shortened distance between Bi^{3+} ions to increase the possibility of non-radiative energy transfer. The emission spectra of La_3TaO_7:0.04Bi^{3+} and La_3SbO_7:0.04Bi^{3+} exhibits a profile of broadband, while their excitation spectra are slightly different (Fig. 3e). By replacing Sb^{5+} with Ta^{5+}, the PL spectra have an obvious blue shift from 530 nm to 462 nm. Interestingly, the emission intensity of La_3TaO_7:0.04Bi^{3+} has increased about 2.6 times than that of La_3SbO_7:0.04Bi^{3+}. As shown in Fig. 3g, the emission intensity slightly decreased initially and then rapidly increased with increasing Ta^{5+} concentration. The peak position showed a rapid blue shift trend followed by a slow redshift, which approaches the peak position of La_3TaO_7:0.04Bi^{3+}. From Fig. 3f, the designed phosphors will appear dual-emission only as the substitution of Ta^{5+} range from 10% to 25%. When the substitution of Ta^{5+} is 20% or 25%, the emission spectra present obvious bimodal emission (Fig. S8 in Supporting information). Besides, the emission intensity locates in the blue-light area demonstrates an increased tendency, as shown in Fig. 3h, which further confirms the effect of Ta^{5+} ions on the local electronic states. Furthermore, the tunable emission of the $La_3Sb_{1-x}Ta_xO_7$:0.04Bi^{3+} sample can be realized by modulating the Ta^{5+} content. Fig. 3i displays the CIE chromaticity coordinate diagram of $La_3Sb_{1-x}Ta_xO_7$:0.04Bi^{3+} samples under 303 nm excitation. The CIE coordinate of the $La_3Sb_{1-x}Ta_xO_7$:0.04Bi^{3+} samples shift from (0.2927, 0.5488) to (0.16619, 0.18315) with the value of x increase from 0 to 1.0. The corresponding luminescence photographs are also presented, which evidently presents the emission color tuning.

Furthermore, the two-wavelength emission may be attributed to two aspects, including the same Bi^{3+} emission center with two radiative decay channels of the excited state and from two Bi^{3+} centers with different local electronic states, which can be further clarified by the PL decay kinetic process. The luminescence lifetime curves of La_3SbO_7:yBi^{3+} ($0.02 \le y \le 0.12$) with different Bi^{3+} contents are measured at room temperature, as displayed in Fig. 4a, which can be fitted with a bi-exponential equation [33]:

$$I(t) = I_0 + A_1 \exp\left(\frac{-t}{\tau_1}\right) + A_2 \exp\left(\frac{-t}{\tau_2}\right) \quad (3)$$

And the average lifetime can be calculated as the following equation:

$$\tau_{avg.} = \frac{A_1\tau_1^2 + A_2\tau_2^2}{A_1\tau_1 + A_2\tau_2} \quad (4)$$

where I_0 and I represent the emission intensity at initial t_0 and time t, A_1 and A_2 denote pre-exponential factors, τ_1 and τ_2 are lifetime components, respectively. As summarized in Table S2 (Supporting information), the average lifetimes of La_3SbO_7:yBi^{3+} monotonously decreased from 296.02 ns to 151.38 ns with increasing y from 0.02 to 0.12.

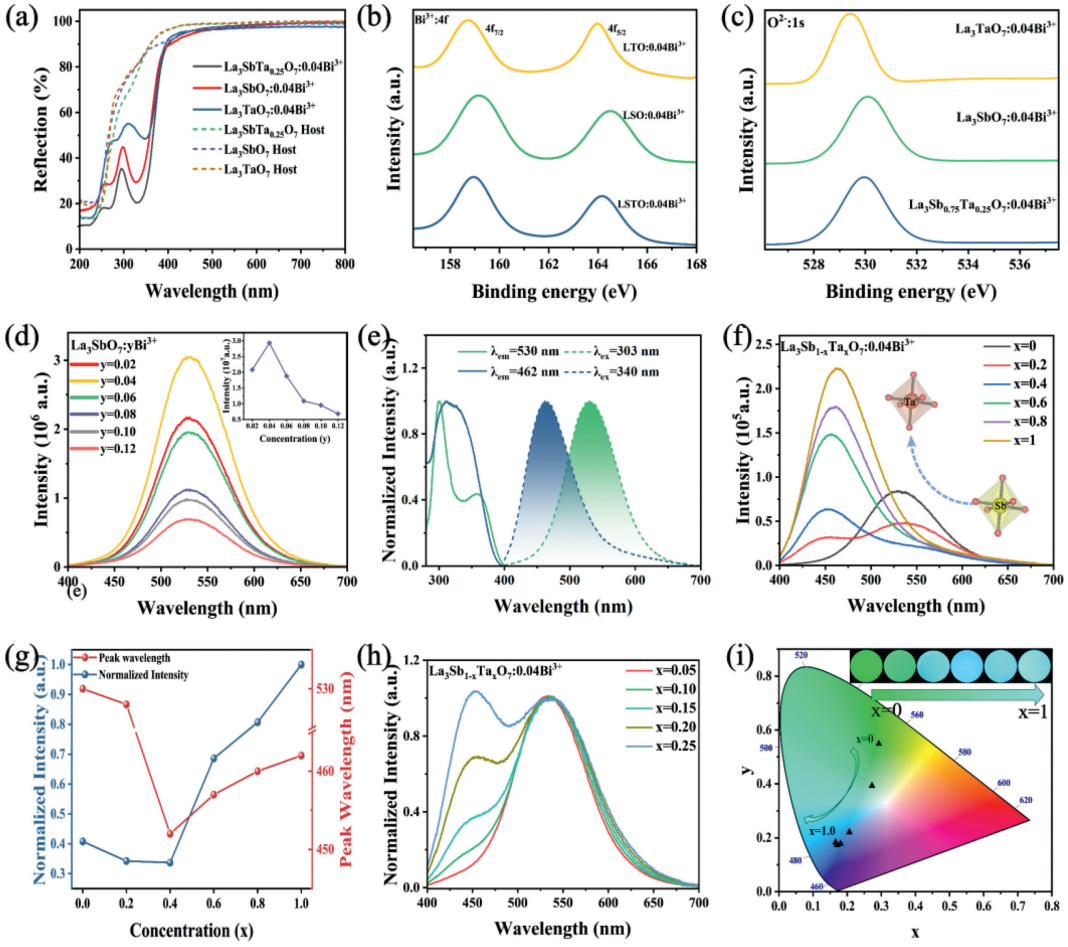

Fig. 3. Optical properties and XPS spectra. (a) The diffuse reflection spectra of the La_3SbO_7, La_3TaO_7, $La_3Sb_{0.75}Ta_{0.25}O_7$ hosts, and the representative Bi^{3+} doped phosphors. (b, c) XPS spectra of the La_3SbO_7:0.04Bi^{3+}, La_3TaO_7:0.04Bi^{3+} and $La_3Sb_{0.75}Ta_{0.25}O_7$:0.04$Bi^{3+}$ samples. (d) PL spectra of the La_3SbO_7:yBi^{3+}($0.02 \le y \le 0.12$). (e) Normalized PL and PLE spectra of the La_3SbO_7:0.04Bi^{3+} and La_3TaO_7:0.04Bi^{3+}. (f) PL spectra of $La_3Sb_{1-x}Ta_xO_7$:0.04Bi^{3+} ($0 \le x \le 1.0$). (g) Normalized PL intensity and the peak position with various Ta^{5+} concentrations. (h) Normalized PL intensity of $La_3Sb_{1-x}Ta_xO_7$:0.04Bi^{3+}($0.05 \le x \le 0.25$). (i) CIE chromaticity coordinates and luminescence photograph of $La_3Sb_{1-x}Ta_xO_7$:0.04Bi^{3+} ($0 \le x \le 1.0$).

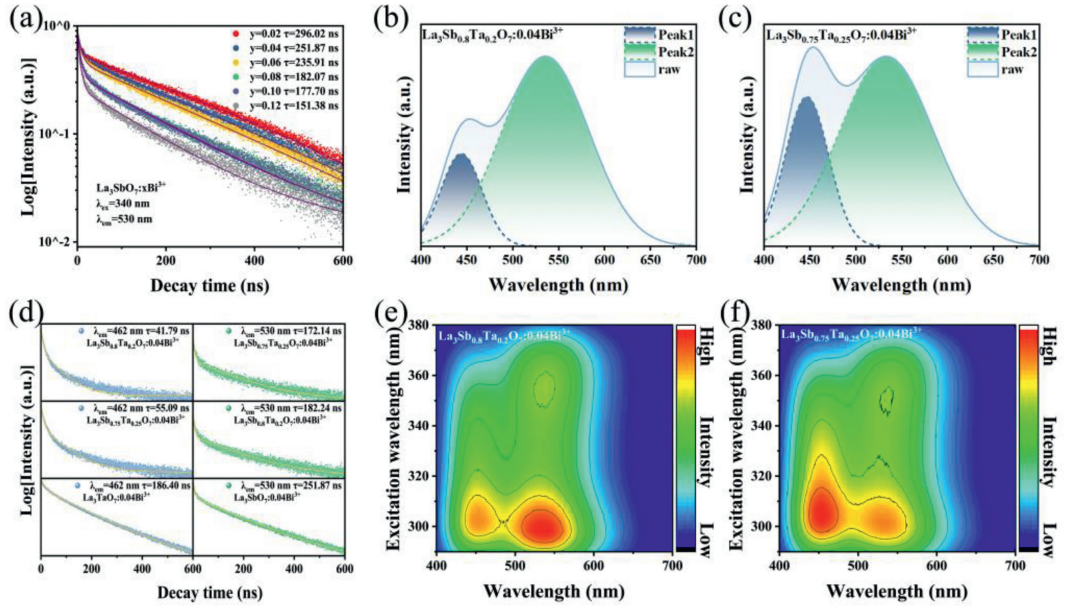

Fig. 4. Properties of bimodal emission. (a) Photoluminescence decay curve of the La_3SbO_7:yBi^{3+} ($0.02 \le y \le 0.12$) under 340 nm excitation. (b, c) Gaussian fitting of PL spectra of $La_3Sb_{0.8}Ta_{0.2}O_7$:0.04Bi^{3+} and $La_3Sb_{0.75}Ta_{0.25}O_7$:0.04$Bi^{3+}$. (d) PL decay curve of the $La_3Sb_{0.8}Ta_{0.2}O_7$:0.04Bi^{3+}, $La_3Sb_{0.75}Ta_{0.25}O_7$:0.04$Bi^{3+}$, La_3SbO_7:0.04Bi^{3+} and La_3TaO_7:0.04Bi^{3+} samples under 340 nm excitation. (e, f) 3D contour map of PL spectra of the $La_3Sb_{0.8}Ta_{0.2}O_7$:0.04Bi^{3+} and $La_3Sb_{0.75}Ta_{0.25}O_7$:0.04$Bi^{3+}$ under different excitation wavelengths.

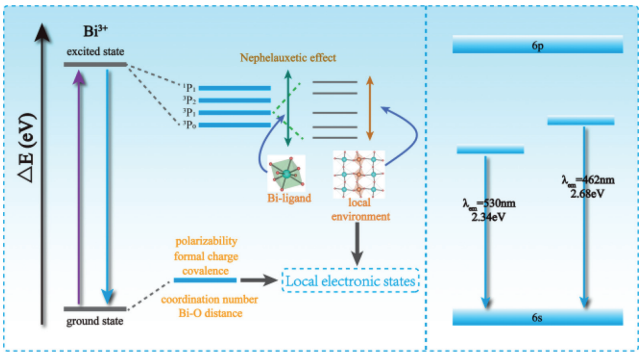

Fig. 5. Schematic energy levels of free Bi^{3+} ion and emission tuning mechanism by changing crystal structure.

From the Gaussian fitting of emission spectra, the broad emission band of $La_3Sb_{0.8}Ta_{0.2}O_7$:0.04Bi^{3+} and $La_3Sb_{0.75}Ta_{0.25}O_7$:0.04$Bi^{3+}$ are both exactly deconvoluted into two peaks at 444 and 535 nm, and at 445 and 530 nm, respectively. Obviously, the PL patterns have changed and the position of the PL peak appears blue-shifted with the substitution of Ta^{5+} ion increased. In general, luminescence lifetime decay is also influenced by the local environment of the emission center. Thus, the luminescence decay curves monitored at 530 and 462 nm with different concentrations of Ta^{5+} ions are presented in Fig. 4d. As the substitution concentration of Ta^{5+} is 20%, the lifetime is calculated to be 41.79 and 182.24 ns monitored at 462 and 530 nm, respectively (Table S3 in Supporting information). While the concentration of Ta^{5+} is 25%, the lifetime is 55.09 and 172.14 ns. These results can be explained by the different local environments of the Bi^{3+} emission centers. From the lifetimes based on different Ta^{5+} concentrations, the substitution of Ta^{5+} for Sb^{5+} enhanced the blue-light emission and weaken the green light emission, which further certifies that the substitution of Ta^{5+} ion can affect the local electronic state around the emission center. In order to confirm the above speculation, two emission peaks with response to different excitation wavelengths are displayed in Figs. 4e and f. As seen from the 3D contour maps of two samples, the long-wavelength emission intensity has a better response to low energy excitation than that of short-wavelength emission intensity with the increase of the excitation wavelength from 290 nm to 380 nm, which is attributed to the different local electronic states around the emission centers.

In general, the PL spectrum of the s-p (Bi^{3+}) transition is related to the crystal field strength, depending on the crystal structure of the host. A new solid solution is created by the substitution of Ta^{5+} to Sb^{5+} with bigger electronegativity and a smaller formal charge, leading to lower polarizability and weaker covalence. That produces a slighter nephelauxetic effect and a weaker crystal field for Bi^{3+} activators. Compared to the original host, the weakening of energy level splitting results in the increase of emission energy, which appears as a blue shift in the spectrum. The crystal field splitting refers to the energy difference between the highest and lowest energy levels, which strongly depends on the coordination situation of activator ions. There is a great influence on the crystal field strength from the bond lengths between activator ions and ligands, the molecular overlap and covalent degree between an activator and its ligands, the coordination environment, and the symmetry of activator-ion sites. In general, the crystal field strength (D_q) in the host can be evaluated by the expression [34]:

$$D_q = \frac{1}{6} Ze^2 \frac{r^4}{R^5} \quad (5)$$

where Z is the valence of the anion, e is the electron charge, r is the wave-function radius, and R is the bond length between the central cation and ligands. As the expression shows, the D_q value is proportional to $1/R^5$, D_q decreases with the increase of R value or polyhedral volume and thus resulting in the emission blue-shift becoming larger. Any change in the composition of the host will change the strength of D_q, which in turn affects the luminescence efficiency, emission peak position, emission color, and PL intensity. These properties provide ideas and schemes for the regulation of Bi^{3+} ions, which makes it possible to tune the emission wavelength by changing the host lattice composition and designing the structure. In the series hosts of $La_3Sb_{0.75}Ta_{0.25}O_7$:0.04$Bi^{3+}$, the homogeneously scattered Ta^{5+} ions have a great influence on the local electronic states, especially around the emission centers. From the specific analysis of fluorescence properties and XPS spectra of Bi^{3+} and O^{2-}, it can be concluded that the substituted Ta^{5+} ion has changed the local electronic states of emission centers, resulting in dual-wavelength emission.

The two emission centers have a great influence on thermal quenching behaviors. Thus, the luminescence spectra of $La_3Sb_{0.8}Ta_{0.2}O_7$:0.04Bi^{3+} and $La_3Sb_{0.75}Ta_{0.25}O_7$:0.04$Bi^{3+}$ with the temperature-dependent from 303 K to 493 K under the 303 nm excitation are studied and illustrated in Figs. 6a-d. The emission intensities from the two emission centers decrease with the temperature rising, owing to the gradually stronger non-radiative effects. Both the blue-light and green-light emissions display decreased intensity with increasing temperature; thus, no obvious correlation is observed between the temperature-dependent behavior of the two emissions. On the contrary, the two emissions display different thermal stability. The thermal stability of green-light emission is obviously better than that of blue-light emission, which further evidences the two emissions from different emission centers. Due to the lower emission intensity and the poorer thermal stability, the blue-light emission of $La_3Sb_{0.8}Ta_{0.2}O_7$:0.04Bi^{3+} completely disappears when the temperature reaches 443 K. Meanwhile, because of the higher emission intensity, $La_3Sb_{0.8}Ta_{0.2}O_7$:0.04Bi^{3+} could hold on to higher temperature (Figs. 6e and f). The thermal quenching mechanism of Bi^{3+} with two local electronic states is illustrated and presented in Figs. 6g and h. The thermal quenching of Bi^{3+} ion occurs through the energy level cross-relaxation (ELCR) between $^1S_0$ and $^3P_1$ states. With increasing the temperature, the electron-phonon coupling is enhanced, and some electrons relax to the intersection of $^1S_0$ and $^3P_1$ states to return to the ground state without radiative transition. The thermal activation energy (E_a) is the difference between the minimum energy of the $^3P_1$ and the intersection [35,36]. The E_a value of blue-light emitting is 0.42 eV, which is smaller than that of green-light emitting. Because Ta^{5+}-substituted influences the energy levels to change the intersection of the two corresponding levels, leading to the two types of thermal quenching behavior. Besides, compared to the blue-light emission center surrounded by bigger [TaO_6], the green-light emission center surrounded by smaller [SbO_6] has tighter cell packing and fewer lattice defects, resulting in higher thermal stability.

Through the peak fitting analysis of the temperature-dependence PL spectra (Figs. S9 and S10 in Supporting information), it is appropriate to adopt a ratio of the integrated emission intensities of the blue-light and green-light energy emission peaks, which can be calculated using as following:

$$I_{green/blue} = \int_{400}^{700} I(\lambda, T) d\lambda \quad (6)$$

where I_{blue} and I_{green} represent the integrated emission intensities of the two emission peaks, respectively. The integration range is the data after Gaussian fitting analysis. As shown in Figs. 6c and f, the trend of the integrated intensity of the emission peak and good discrimination dual-wavelengths illustrate the possibil-

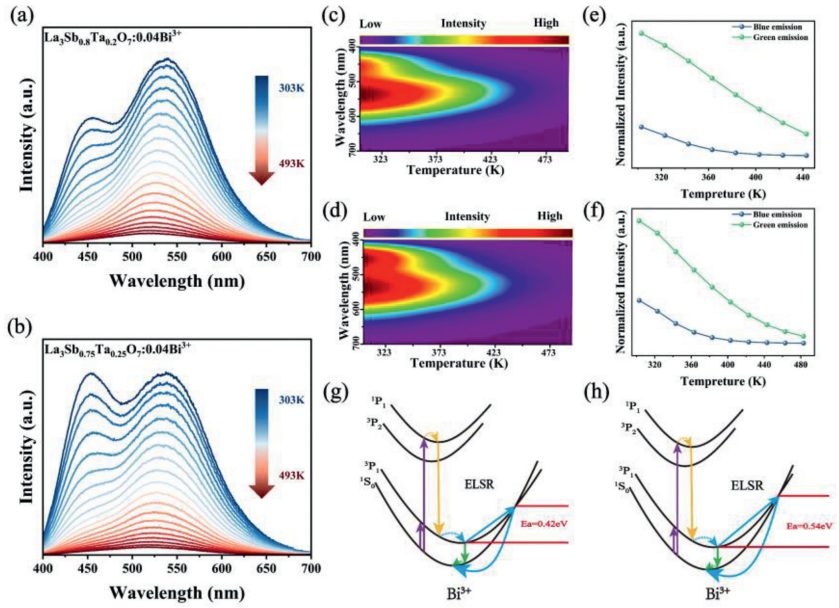

Fig. 6. Temperature-dependent characteristics of $La_3Sb_{0.8}Ta_{0.2}O_7$:0.04Bi^{3+} and $La_3Sb_{0.75}Ta_{0.25}O_7$:0.04$Bi^{3+}$. (a, b) PL spectra from 303 K to 493 K, and (c, d) the corresponding two-dimension images. (e, f) Normalized emission intensity. (g, h) The quenching mechanism for the Bi^{3+} activator with blue-light and green-light emitting.

ity for optical temperature sensing based on FIR strategy. Herein, the visual dual-wavelength emitting $La_3Sb_{0.8}Ta_{0.2}O_7$:0.04Bi^{3+} and $La_3Sb_{0.75}Ta_{0.25}O_7$:0.04$Bi^{3+}$ materials are chosen to further test the temperature-dependent property. A ratiometric fluorescence sensor can detect temperature based on the dual wavelength with different thermal-quenching performances.

The relationship of the *FIR* (I_{blue}/I_{green}) and temperature can be described as follows [37]:

$$FIR(T) = \frac{I_{blue}}{I_{green}} = A/(1 + Bexp(-C/T)) \quad (7)$$

where T refers to the absolute temperature; A, B and C denote the related constant parameters. In the field of luminescence thermometry, the absolute sensitivity (S_a) and relative sensitivity (S_r) are requisite parameters to measure the temperature performance, which can be calculated by the following equations:

$$S_a = \left|\frac{\partial FIR}{\partial T}\right| = ABexp(-C/T) \times \frac{C}{T^2} \quad (8)$$

$$S_r = 100\% \times \left|\frac{1}{FIR}\frac{\partial FIR}{\partial T}\right| = 100\% \times \frac{ABexp(-C/T)}{A/(1 + Bexp(-C/T))} \times \frac{C}{T^2} \quad (9)$$

As presented in Fig. 7a, the relation between *FIR* and temperature of $La_3Sb_{0.8}Ta_{0.2}O_7$:0.04Bi^{3+} can be expressed by the following formula:

$$FIR = 0.286/(1 + 884431.7)\exp(-4612.8/T) \quad (10)$$

Furthermore, as displayed in Fig. 7c, in the sample of $La_3Sb_{0.75}Ta_{0.25}O_7$:0.04$Bi^{3+}$, the relation can between *FIR* and temperature is expressed by the following formula:

$$FIR = 0.445/(1 + 43956.02)\exp(-3645.5/T) \quad (11)$$

As demonstrated in Figs. 6b and d, the value of S_a and S_r increase initially and then reduce with the temperature increasing from 303 to 493 K. The maximum S_a value of $La_3Sb_{0.8}Ta_{0.2}O_7$:0.04Bi^{3+} reaches 0.00297 K^{-1} at 330 K, while the S_r is 2.64%/K at 383 K. In contrast, the maximum S_a value of

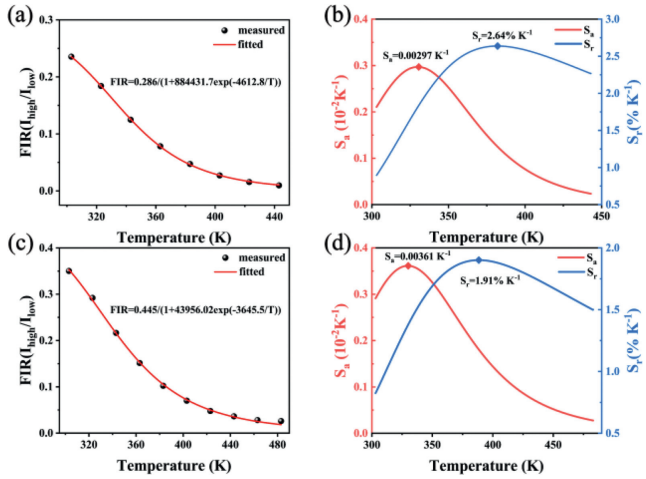

Fig. 7. Temperature measurement performance. (a) *FIR* (I_{blue}/I_{green}) of $La_3Sb_{0.8}Ta_{0.2}O_7$:0.04Bi^{3+}between 303 K and 443 K. (b) The corresponding S_a and S_r values. (c) *FIR* (I_{blue}/I_{green}) of $La_3Sb_{0.75}Ta_{0.25}O_7$:0.04$Bi^{3+}$ between 303 K and 483 K. (d) The corresponding S_a and S_r values are calculated between 303 K and 483 K.

$La_3Sb_{0.75}Ta_{0.25}O_7$:0.04$Bi^{3+}$ achieves 0.00361 K^{-1} at 330 K, and the S_r reaches the maximum of 1.91%/K at 388 K. Based on the analysis of temperature performance and thermal stability, the designed $La_3Sb_{0.8}Ta_{0.2}O_7$:0.04Bi^{3+} phosphor has a higher S_r, but a narrower temperature measurement interval, compared with that of $La_3Sb_{0.75}Ta_{0.25}O_7$:0.04$Bi^{3+}$.

Moreover, the temperature resolution (δ_T) is a thermometric parameter to evaluate the accuracy of the designed phosphors, which can be calculated by the following formula [38,39]:

$$\delta T = \frac{1}{S_r}\frac{\delta FIR}{FIR} \quad (12)$$

where δ_{FIR} is determined to be the standard deviation for 30 circulations at room temperature, and $\delta_{FIR/FIR}$ refers to the relative error in the determination of the thermometric parameter (Figs. S11 and S12 in Supporting information). Results demonstrate that both temperature resolution of the developed $La_3Sb_{0.8}Ta_{0.2}O_7$:0.04Bi^{3+}

and $La_3Sb_{0.75}Ta_{0.25}O_7$:0.04$Bi^{3+}$ samples are below 0.005 K in the temperature range from 273 K to 383 K, and the maximum resolution is up to 0.023 K and 0.0119 K, respectively.

The emission spectral of the $La_3Sb_{0.8}Ta_{0.2}O_7$:0.04Bi^{3+} covered the blue-and-green area, which matches the demand of w-LED (white light-emitting diode). Therefore, we constructed a w-LED device using commercial red phosphors on an n-UV LED chip to evaluate the potential application [40,41]. A continuous broad emission from blue to red and emit warm lights can be obtained (Fig. S13 in Supporting information). The CCT and CRI of the fabricated w-LED are found to be 3482 K and 87.8, respectively. The photoelectric performance reveals the designed phosphors have potential application towards w-LED.

In summary, a series of blue-green color-tunable $La_3Sb_{1-x}Ta_xO_7$:Bi^{3+} ($0 \le x \le 1.0$) phosphors were designed by the cationic substitution strategy. With the replacement of Ta^{5+} to Sb^{5+}, the emission tremendously shifted from green to blue with 68 nm and the intensity was enhanced 2.6 times. Besides, as the Ta^{5+} substation concentration at 20% or 25%, a novel dual-wavelength emitting phosphor was achieved for optical temperature sensing based on the two emission centers with two local electronic states from Bi^{3+}-doped $La_3Sb_{1-x}Ta_xO_7$ ($0 \le x \le 1.0$) solid solution. The two local electronic states corresponding to the emission centers were managed *via* cationic substitution for realizing the dual-wavelength emitting of Bi^{3+} ions in the single host. The two emission peaks from their emission centers have distinguished thermal-quenching behaviors, which were further applied in the FIR optical temperature sensing. The dual-wavelength emitting peaks of $La_3Sb_{0.8}Ta_{0.2}O_7$:0.04Bi^{3+} and $La_3Sb_{0.75}Ta_{0.25}O_7$:0.04$Bi^{3+}$ phosphors have different temperature-dependent emission characteristics, where the S_a and S_r were both discussed in the temperature range from 303 K to 483 K. The maximum values of S_r reach 2.64%/K ($La_3Sb_{0.8}Ta_{0.2}O_7$:0.04Bi^{3+}@383 K) and 1.91%/K ($La_3Sb_{0.75}Ta_{0.25}O_7$:0.04$Bi^{3+}$@388 K), relatively. The design of local electronic state modulation will provide a new strategy for developing novel multifunctional phosphors.

Declaration of competing interest

The authors declare that they have no known competing financial interests or personal relationships that could have appeared to influence the work reported in this paper.

Acknowledgments

This work was supported by the National Natural Science Foundation of China (Nos. 52072101, 51972088, 52172205), the Fundamental Research Funds for the Provincial Universities of Zhejiang (No. GK229909299001-003), the Postgraduate Research Innovation Fund of Hangzhou Dianzi University (No. CXJJ2022032).

Supplementary materials

Supplementary material associated with this article can be found, in the online version, at doi:10.1016/j.cclet.2023.108447.

References

[1] C.D.S. Brites, S. Balabhadra, L.D. Carlos, Adv. Opt. Mater. 7 (2019) 1801239.
[2] G. Kucsko, P.C. Maurer, N.Y. Yao, et al., Nature 500 (2013) 54–58.
[3] G. Li, G. Li, Q. Mao, et al., Chem. Eng. J. 430 (2022) 132923.
[4] B. Deng, S. Liu, C. Zhou, et al., Chem. Eur. J. 24 (2018) 11627.
[5] P. Du, J. Tang, W. Li, L. Luo, Chem. Eng. J. 406 (2021) 127165.
[6] Y. Gao, Y. Bando, Nature 415 (2002) 599.
[7] G. Bao, K.L. Wong, D. Jin, P.A. Tanner, Light Sci. Appl. 7 (2018) 96.
[8] X. Qiu, Q. Zhou, X. Zhu, et al., Nat. Commun. 11 (2020) 4.
[9] J.R. Shakirova, N.N. Shevchenko, V.A. Baigildin, et al., ACS Appl. Polym. Mater. 2 (2020) 537–547.
[10] M. Xu, X. Zou, Q. Su, et al., Nat. Commun. 9 (2018) 2698.
[11] M.A. Hernández-Rodríguez, A.D. Lozano-Gorrín, I.R. Martín, U.R. Rodríguez-Mendoza, V. Lavín, Sens. Actuators B 255 (2018) 970–976.
[12] G. Li, Y. Xue, Q. Mao, et al., Dalton Trans. 51 (2022) 4685–4694.
[13] W. Liu, X. Wang, Q. Zhu, et al., Sci. Technol. Adv. Mater. 20 (2019) 949–963.
[14] S.W. Long, S.P. Lin, D.C. Ma, et al., Photonics Res. 8 (2020) 135–142.
[15] Miroslav D. Dramićanin, J. Appl. Phys. 128 (2020) 040902.
[16] D. Liu, X. Yun, P. Dang, et al., Chem. Mater. 7 (2020) 3065–3077.
[17] R.M. Friedman, J.D. Corbett, Inorg. Chem. 12 (1973) 1134–1139.
[18] Y. Wang, J. Ding, Y. Wang, J. Am. Ceram. Soc. 100 (2017) 2612–2620.
[19] L. Seijo, Z. Barandiaran, Phys. Chem. Chem. Phys. 16 (2014) 17305–17314.
[20] F. Kang, M. Peng, D. Lei, Q. Zhang, Chem. Mater. 28 (2016) 7807–7815.
[21] M. Zhao, H. Liao, M. Molokeev, et al., Light Sci. Appl. 8 (2019) 38.
[22] F. Kang, G. Sun, P. Boutinaud, et al., J. Mater. Chem. C 7 (2019) 9865–9877.
[23] Y. Wei, Z. Gao, X. Yun, et al., Chem. Mater. 32 (2020) 8747–8753.
[24] P. Dang, D. Liu, G. Li, A. Kheraif, J. Lin, Adv. Opt. Mater. 8 (2020) 1901993–1902005.
[25] D. Liu, P. Dang, X. Yun, et al., J. Mater. Chem. C 7 (2019) 13536–13547.
[26] X. Shi, Y. Xue, Q. Mao, et al., Inorg. Chem. 62 (2023) 893–903.
[27] M. Jain, P. Rajput, A. Vij, A. Thakur, J. Mater. Chem. C 10 (2022) 11379–11387.
[28] F. Massee, Y.K. Huang, M. Aprili, Science 367 (2020) 6473.
[29] P. Gao, Q. Li, C. Zhou, et al., Inorg. Chem. 61 (2022) 13104–13114.
[30] Y. Wei, L. Cao, L. Lv, et al., Chem. Mater. 30 (2018) 2389–2399.
[31] Q. Ma, G. Ning, Y. Xin, B. Shao, Inorg. Chem. Front. 8 (2021) 4072–4085.
[32] B. Li, Z. Li, X. Wu, Z. Zhu, Nano Res. Energy 1 (2022) 9120011.
[33] X. Shi, M. Zhang, X. Lu, et al., Mater. Today Chem. 27 (2023) 101264.
[34] G. Li, Y. Zhao, Y. Wei, et al., Chem. Commun. 52 (2016) 3376–3379.
[35] B. Zhao, Y. Chen, Y. Xue, et al., Mater. Des. 227 (2023) 111802.
[36] Y. Ding, N. Guo, M. Zhu, et al., Mater. Res. Bull. 129 (2020) 110869.
[37] J. Jin, J. Lin, Y. Huang, et al., Chin. Chem. Lett. 33 (2022) 4798–4802.
[38] Y. Wang, Y. Sun, Z. Xia, J. Phys. Chem. Lett. 14 (2023) 178–182.
[39] T. Hu, Y. Gao, M. Molokeev, Z. Xia, Q. Zhang, Sci. China Mater. 62 (2019) 1807–1814.
[40] T. Li, Y. Zheng, C. Wu, et al., Chin. Chem. Lett. 33 (2022) 4238–4242.
[41] J. Yang, C. Lei, X. Liu, et al., Acta Phys. Chim. Sin. 38 (2022) 2111020.